Since January 2020 Elsevier has created a COVID-19 resource centre with free information in English and Mandarin on the novel coronavirus COVID-19. The COVID-19 resource centre is hosted on Elsevier Connect, the company's public news and information website.

Expert Systems With Applications 185 (2021) 115650

Contents lists available at ScienceDirect

Expert Systems With Applications

journal homepage: www.elsevier.com/locate/eswa

Wavelet and deep learning-based detection of SARS-nCoV from thoracic X-ray images for rapid and efficient testing

Amar Kumar Verma [a], Inturi Vamsi [b], Prerna Saurabh [c], Radhika Sudha [a,*], Sabareesh G.R. [b], Rajkumar S. [c]

[a] Department of Electrical and Electronics, Birla Institute of Technology and Science-Pilani, Hyderabad Campus, 500078, India
[b] Department of Mechanical Engineering, Birla Institute of Technology and Science-Pilani, Hyderabad Campus, 500078, India
[c] Department of Computer Science and Engineering, Vellore Institute of Technology-Vellore Campus, Tamil Nadu, 632014, India

ARTICLE INFO

Keywords:
Medical imaging
Wavelets
rRT-PCR
COVID-19
Transfer learning

ABSTRACT

This paper proposes a wavelet and artificial intelligence-enabled rapid and efficient testing procedure for patients with Severe Acute Respiratory Coronavirus Syndrome (SARS-nCoV) through a deep learning approach from thoracic X-ray images. Presently, the virus infection is diagnosed primarily by a process called the real-time Reverse Transcriptase–Polymerase Chain Reaction (rRT-PCR) based on its genetic prints. This whole procedure takes a substantial amount of time to identify and diagnose the patients infected by the virus. The proposed research uses a wavelet-based convolution neural network architectures to detect SARS-nCoV. CNN is pre-trained on the ImageNet and trained end-to-end using thoracic X-ray images. To execute Discrete Wavelet Transforms (DWT), the available mother wavelet functions from different families, namely Haar, Daubechies, Symlet, Biorthogonal, Coiflet, and Discrete Meyer, were considered. Two-level decomposition via DWT is adopted to extract prominent features peripheral and subpleural ground-glass opacities, often in the lower lobes explicitly from thoracic X-ray images to suppress noise effect, further enhancing the signal to noise ratio. The proposed wavelet-based deep learning models of both, two-class instances (COVID vs. Normal) and four-class instances (COVID-19 vs. PNA bacterial vs. PNA viral vs. Normal) were validated from publicly available databases using k-Fold Cross Validation (k-Fold CV) technique. In addition to these X-ray images, images of recent COVID-19 patients were further used to examine the model's practicality and real-time feasibility in combating the current pandemic situation. It was observed that the Symlet 7 approximation component with two-level manifested the highest test accuracy of 98.87%, followed by Biorthogonal 2.6 with an efficiency of 98.73%. While the test accuracy for Symlet 7 and Biorthogonal 2.6 is high, Haar and Daubechies with two levels have demonstrated excellent validation accuracy on unseen data. It was also observed that the precision, the recall rate, and the dice similarity coefficient for four-class instances were 98%, 98%, and 99%, respectively, using the proposed algorithm.

1. Introduction

The outbreak of the contagious disease COVID-19, which was declared a pandemic by WHO in late 2019 and early 2020, impacted humanity and the global economy. The epidemic is thought to have originated in December 2019 in Wuhan, Hubei Province, China (Ma, 2020). COVID-19 is caused by a virus that belongs to the Coronaviridae subfamily of the order Nidovirales. Severe acute respiratory syndrome, Middle East Respiratory Syndrome (MERS), and COVID-19 are all driven by these viruses (Organization, 2020; Sohrabi et al., 2020). COVID-19 is a new form of the virus that produces a variety of symptoms. It is classified as SARS-CoV-2. Fever, dry cough, tiredness, fatigue, headache, sore throat, muscular pain, diarrhea, loss of taste or smell, skin rash, myalgias, shortness of breath, thoracic discomfort, loss of speech or movement, respiratory sickness are only a few of the symptoms. Severe infection can cause pneumonia, heart damage, multi-organ failure, and death in certain individuals (W.H.O., 2020). The virus transmits from person to person through the droplet of an infected individual's sneeze or cough due to its infectious nature. Furthermore, if an infected person contacts the droplet and inhales the virus-laden

* Corresponding author.
E-mail addresses: p20170423@hyderabad.bits-pilani.ac.in (A.K. Verma), p20160025@hyderabad.bits-pilani.ac.in (I. Vamsi), prerna.saurabh2019@vitstudent.ac.in (P. Saurabh), sradhika@hyderabad.bits-pilani.ac.in (R. Sudha), sabareesh@hyderabad.bits-pilani.ac.in (Sabareesh G.R.), rajkumars@vit.ac.in (Rajkumar S.).

https://doi.org/10.1016/j.eswa.2021.115650
Received 21 February 2021; Received in revised form 2 June 2021; Accepted 20 July 2021
Available online 2 August 2021

air, the second person may get the infection quickly. According to the World Health Organization, Globally, as of 5:06pm CEST, 1 June 2021, there have been 17,04,26,245 confirmed cases of COVID-19, including 35,48,628 deaths, reported to WHO. As of 30 May 2021, a total of 157,94,16,705 vaccine doses have been administered (Worldometer, 2020). Because the development of a vaccine is still in its early stages, early detection of COVID-19 illness is critical for reducing and controlling the spread of the disease (Catanzaro, Fagiani, Racchi, Corsini, Govoni, & Lanni, 2020). If a patient is infected, they must be isolated as soon as possible to prevent the infection from spreading further. Currently, the process known as reverse transcription-polymerase chain reaction (RT-PCR) is utilized for testing and diagnosing whether or not a person is infected with COVID-19 (Corman et al., 2020; Mei et al., 2020; Patchsung et al., 2020; Wang, Xu et al., 2020). The respiratory samples are used in this test, and the results are available in four to eight hours. Rapid diagnostic tests (RDT), enzyme-linked immunosorbent assay (ELISA), neutralization assays, chemiluminescent immunoassays, and binding antibodies are all used in certain antibody studies to detect COVID-19. Many health organizations, however, employ a thoracic X-ray scan image to diagnose lung disease on occasion. Most nations ran out of testing kits in the early phases of the COVID-19 outbreak. In comparison to the RT-PCR results (low sensitivity, 60%–70%), the CT images-based lab test (sensitivity, 98%) showed promising findings for the COVID-19 infection rate (Fang et al., 2020; Harmon et al., 2020). Moreover, a few studies claim that lab reports and clinical image aspects are even better for early COVID-19 identification (Lee, Ng, & Khong, 2020; Long et al., 2020; Shi et al., 2020).

Many health organizations recommend thoracic X-ray imaging as a promising alternative for early COVID-19 screening (Bressem, Adams, Erxleben, Hamm, Niehues, & Vahldiek, 2020). With the developments in AI, the advancements in pattern recognition and machine learning can be exploited to automate the detection of COVID-19 from the X-ray images (Greenspan, Estépar, Niessen, Siegel, & Nielsen, 2020; Luengo-Oroz et al., 2020; Ting, Carin, Dzau, & Wong, 2020). In the past, deep learning-based methods have provided encouraging results in the medical field such as breast cancer detection (Celik, Talo, Yildirim, Karabatak, & Acharya, 2020; Cruz-Roa et al., 2014), skin cancer classification (Codella et al., 2017; Esteva et al., 2017), brain disease classification (Talo, Yildirim, Baloglu, Aydin, & Acharya, 2019), arrhythmia detection (Hannun et al., 2019), pneumonia detection from X-ray images (Rajpurkar et al., 2017), and lung segmentation (Gaál, Maga, & Lukács, 2020; Souza, Diniz, Ferreira, da Silva, Silva, & de Paiva, 2019). An accurate, fast, and efficient model using a wavelet-based deep learning model is proposed to detect covid infection automatically. The proposed work uses wavelet-based convolution neural network architectures to detect SARS-nCoV. CNN is pre-trained on the ImageNet and trained end-to-end using thoracic X-ray images. Two-level decomposition via DWT is adopted to extract prominent features explicitly from thoracic X-ray images of publicly accessible databases to detect SARS-nCoV. Many past studies have reported the use of deep learning techniques in detecting diseases at an early stage. The scientific community has tried to extend this learning in their fight against the coronavirus. Early detection can reduce the severity of an affected person and prevent further spreading by isolating the affected person.

2. Literature survey

COVID-19 detection from thoracic X-ray imaging and computed tomography images is the focus of many of these studies in the literature. To identify SARS-nCoV, the conventional strategy primarily employs a process known as transfer-learning. Typically, limited data sets are used to perform the transfer learning approach. Transfer learning takes knowledge from a large collection of data acquired by CNNs and applies it to a new data set to complete other comparable tasks. In the beginning, CNNs are trained to extract the most notable features from a large-scale dataset for certain tasks and outcomes. Their efficiency is evaluated to determine if it is suitable for transfer learning. This pre-trained CNN is then utilized to extract features from a new set of images via transfer learning while keeping both its initial architecture and the weights it has learned. After that, the new model is utilized for classification. This technology would have a substantial influence on automated X-ray image identification and retrieval for SARS-nCoV detection. AlexNet, VGG-16, VGG-19, SqueezeNet, GoogleNet, MobileNet-V2, ResNet-18, ResNet-50, ResNet-101, and Xception were employed in the majority of earlier research (Minaee, Kafieh, Sonka, Yazdani, & Soufi, 2020).

Xu et al. (2020) introduced ResNet-18 pre-trained network with an architecture for location attention. This research aimed to develop an early screening model to identify COVID-19 pneumonia from Influenza-A-viral pneumonia (IAVP) and healthy cases through pulmonary CT images using deep learning techniques. Finally, the type of infection and the overall confidence score for each CT case were determined using the Noisy- or Bayesian function. Zhang, Xie, Li, Shen and Xia (2020) mentioned a concise duration of cluster formation in viral pneumonia. This paper has used the classification of one class to tackle the problem of anomaly detection. It uses Confidence-Aware Anomaly Detection (CAAD) mode to differentiate viral pneumonia from non-viral pneumonia. This model has different roles, such as extractor feature, anomaly detector, and predictor of confidence. If the detector of anomaly scores large or the predictor of confidence is small, the model accepts the instance as an input indicating viral pneumonia. This model takes all cases of viral pneumonia rather than taking individual cases as anomalies. Wang and Wong (2020) proposed the COVID-Net and deep CNN that aims to make the right prediction based on their methods to give better results in the screening process. It also promises to provide valid information from the CXR images. Salman, Abu-Naser, Alajrami, Abu-Nasser, and Alashqar (2020) used an inception v3 architecture for two-class instances (COVID-19 and non-COVID) and got an accuracy of 100%. The main drawbacks of this method were that they used a small dataset and ignored the SARS, MERS, and ARDS images. Sethy and Behera (2020) have proposed a ResNet 50 and SVM model that can detect patients infected by the COVID using X-ray images using a deep feature technique that could be useful for medical practitioners. Wang, Kang et al. (2020) proposed DenseNet121 architecture to characterize the COVID-19 images and found multiple factors responsible for identifying patients with COVID or finding high-risk patients. The deep learning system automatically focused on suspicious areas that displayed conflicting characteristics with reported radiological findings without human intervention. Narin, Kaya, and Pamuk (2020) proposed an automated system be introduced to diagnose people infected with COVID-19 using the CNN model that uses ResNet-50, InceptionV3, InceptionResNetV2 X-ray images. This model uses an uncertainty matrix to show a 5-fold cross-validation technique. It is demonstrated that the pre-trained ResNet50 model provides the best accuracy in classification compared to the other two methods proposed. Gozes et al. (2020) used a lung segmentation module to extract the features and ResNet-50 architecture for classification, achieving a sensitivity of 94% and specificity of 98%. This paper proposed a framework that utilizes robust 2D and 3D deep learning models, modifying and adapting existing AI models and combining them with clinical understanding. Many retrospective studies are being performed to understand and analyze the COVID patients diagnosed and estimate each patient's disease evolution. Apostolopoulos and Mpesiana (2020) aimed to evaluate the performance of a state-of-the-art CNN architecture proposed over the years for medical image classification. VGG-19 architecture was used for the automatic diagnosis of COVID-19 from the thoracic X-rays. Barstugan, Ozkaya, and Ozturk (2020) used a range of extraction methods such as Gray Level Co-occurrence Matrix, Local Directional Pattern, Gray Level Run Length Matrix, Gray-Level Size Zone Matrix, and Discrete Wavelet Transform algorithms. Using the function, an accuracy of 99.68% was achieved using this method.

The circumstances shown by CT images (bronchiectasis, signs of lesion swelling, shadowing, etc.) provide a simple diagnosis of COVID-19. It has also used cross-validation 2-fold, 5-fold, and 10-fold. Hemdan, Shouman, and Karar (2020) have introduced a new paradigm for a pre-trained deep learning classifier, i.e., COVIDX-Net, to help radiologists classify or validate COVID-19 2D X-ray images automatically.

DCNNs are used to identify common thoracic diseases in CT images, such as Tuberculosis screening and mediastinal lymph nodes. However, its COVID-19 detection application is still limited. Those DCNNs model are: VGG19, MobileNetV2, Xception, InceptionResNetV2, InceptionV3, ResNetV2 and DenseNet121. Each deep neural network model will analyze the normalized intensities and ground-glass opacity of the X-ray images to identify the patient status in either negative or positive COVID-19 instances. A summary of the COVID-19 detection methods using thoracic X-ray and CT images is elaborated in Table 1. It shows that many methods depend on the transfer learning and used a minimal dataset. There is a broader scope for improving the classification efficiency using tested and proved models that can use wavelet-based feature extraction. Wavelet Transform (WT) measures the correlation between the input image and the mother Wavelet through an adaptable 2D time-scale window. It performs the translation (time-domain) and dilation (scaling) to decompose the signal into a series of wavelet coefficients. Due to its multi-resolution property, WT can capture the change in the transient energy phenomenon contained by the signal/image. Thus, it has various applications in anomaly detection, edge detection, signal, and image processing (Inturi, Sabareesh, & Penumakala, 2020; Wang & Du, 2019). Discrete Wavelet Transform (DWT) decomposes the input image into a set of approximation and detail coefficients. Further, each previous level approximation coefficient is subjected to the next level of decomposition and so on. Various authors have executed the DWT algorithm to de-noise the raw signals captured through multiple sensors and accomplished the fault diagnosis in various rotating machinery such as gearbox and motors (Radhika, Sabareesh, Jagadanand, & Sugumaran, 2010; Radhika, Tamura, & Matsui, 2015; Vamsi, Sabareesh, & Penumakala, 2019). Praveen, Vamsi, Suresh, and Radhika (2020) performed three-level DWT decomposition and extracted statistical indicators from the sub-images to evaluate the surface roughness of formed specimens. Nazarahari, Namin, Markazi, and Anaraki (2015) decomposed the electrocardiography signals through four-level DWT and generated a feature vector database. The authors have further classified the feature vector database through the multilayer perceptron algorithm to distinguish between the various cardiac arrhythmias. Chakraborty and Nandy (2020) have combined the DWT and deep neural network algorithms to classify the pathological gait abnormality pattern.

3. Methodology

Discrete wavelet transforms or DWT implements a combination of low-pass $\phi(t)$ and high-pass $\psi(t)$ filters to achieve the approximation and detail wavelet coefficients, respectively, by down sampling the input image. Thus, a single DWT level convolutes each row and column of the input image data matrix to obtain a set of four fine-scale sub-images. The direction of the convolution of rows and columns of an input image through the low and high-pass filters represents wavelet coefficients' orientation. As described in Fig. 1, the convolution of the low-pass filter (LPF) initially on the rows of input image followed by the columns of the image could result in approximation wavelet coefficients (A1) (Radhika, Tamura, & Matsui, 2012). Similarly, the convolution of the LPF on the rows and high-pass filter (HPF) on the columns of the image could generate the horizontal detail wavelet coefficients (hD1). Also, vertical detail coefficients (vD1) are formed by the convolution of HPF on the rows, followed by an LPF on the image columns. Finally, the HPF's convolution on the rows, followed by the columns of the image, generates the diagonal detail wavelet coefficients (dD1). The approximation coefficients of the first level (sub-image A1) is further decomposed to achieve the next level coarse scaled wavelet coefficients, i.e., A2, hD2, vD2 & dD2, and A2 sub-image is downsampled to the next level, and this iteration continues further.

Mathematically, DWT is expressed as,

$$DWT(x,y) = \frac{1}{\sqrt{2^p}} \int_{-\infty}^{+\infty} s(t)\psi^* \left(\frac{t - 2^p q}{2^p} \right) dt \tag{1}$$

$$\phi(t) = \sqrt{2} \sum_{y} a(y)\phi(2t - y) \tag{2}$$

$$\psi(t) = \sqrt{2} \sum_{y} d(y)\phi(2t - y) \tag{3}$$

DWT (x, y) are the wavelet coefficients, ψ is the base wavelet function, ψ^* is the complex conjugate of the base wavelet function, and p, q are the integers corresponding to scale and translation, respectively. Thus, the approximation and detail wavelet coefficients are achieved by convoluting the input image with the scale function and wavelet function represented in Eqs. (2) and (3) respectively.

Kumar Singh, Abdel-Nasser, Pandey, and Puig (2021) have proposed a Discrete Wavelet Transform (DWT) in conjunction with deep-learning based method and segmented the COVID-19 infected regions from the lung Computed Tomography (CT) images. However, the investigation is primarily focussed on a single case, i.e., COVID-19 CT image data. Rajpal, Lakhyani, Singh, Kohli, and Kumar (2021) have used a deep convolutional neural network (ResNet-50) to learn the features from the chest X-ray images and distinguished among the three classes, namely, normal, COVID-19 and pneumonia. Gungor (2021) de-noised the CT images through DWT using various mother wavelets and diagnosed the COVID-19 disease. It was observed that, the second-level approximation coefficients of Daubechies (db3) wavelet have yielded better results among the other mother wavelets. Chaudhary and Pachori (2021) implemented wavelet packet transform on the chest CT images and X-ray images in conjunction with pre-trained convolutional neural network to classify among the healthy, COVID-19 and pneumonia conditions.

Previous studies have identified the appropriate base wavelet function by examining the energy distribution of the 1-D signal at various bands of frequency (Balavignesh, Gundepudi, Sabareesh, & Vamsi, 2018). However, the same criteria may not perform while analyzing the 2-D image. Therefore, in this investigation, all the available base wavelet functions from various families, namely, Haar, Daubechies, Symlet, Biorthogonal, Coiflet, and Discrete Meyer, are considered for executing the DWT. Two-level decomposition through DWT is adopted to suppress noise's influence on the input image, further enhancing the signal-to-noise ratio. Initially, image augmentation is performed, and four images in the bands of red, green, blue, and gray-scale format are individually retrieved from the single input image. Later, two-level DWT is implemented on all the retrieved format of image formats, and various sub-images in the form of wavelet coefficients are achieved. Thus, a total of thirty-two sub-images (4 bands * 2 levels * 4 wavelet coefficients) are obtained from a single input image. A similar procedure is implemented on all the images from the four different health conditions (classes) such as normal, viral pneumonia, pneumonia bacterial, and COVID-19 is as shown in Fig. 2, and various sub-images in the form of wavelet coefficients are achieved. Further, the obtained sub-images are channeled as input to the CNN algorithm to distinguish between the different health conditions.

Previous radiological studies have shown that image features, such as Ground-Glass Opacity (GGO) or mixed GGO and consolidation, are identical in most cases. Coronavirus disease 2019 pneumonia with bilateral, multifocal lower-lung involvement (Chung et al., 2020; Kanne, 2020; Song, Shi et al., 2020) is anticipated to have a peripheral spread. Despite negative reverse-transcription polymerase chain reaction findings, viral pneumonia features may be highly suspicious for COVID-19 infection in the sense of standard clinical presentation and exposure to other individuals with COVID-19. Repeat swab monitoring and patient isolation should be examined in these circumstances. An appropriate base wavelet function is required to decompose the input image through DWT as shown in Figs. 3 and 4.

Table 1
Summary of the COVID-19 detection and diagnostic methods for thoracic X-ray and CT image.

Authors	Image modality	Method used	COVID-19 positive cases	Accuracy (in %)
Xu et al. (2020)	CT images	ResNet-18 + location attention	219 (+)	86.70
Zhang, Satapathy et al. (2020)	X-ray images	ResNet-18 + classification head + anomaly detection head	100 (+)	96.00
Wang and Wong (2020)	X-ray images	COVID-Net	53 (+)	92.40
Sethy and Behera (2020)	X-ray images	ResNet50+SVM	25 (+)	95.38
Wang, Zha et al. (2020)	CT images	DenseNet121	924 (+)	80.12
Narin et al. (2020)	X-ray images	Deep CNN ResNet-50	50 (+)	98.00
Gozes et al. (2020)	CT images	ResNet-50	50 (+)	94.00
Apostolopoulos and Mpesiana (2020)	X-ray images	VGG-19	244 (+)	93.48
Abbas, Abdelsamea, and Gaber (2020)	X-ray images	DeTrac	105 (+)	95.12
Hall, Paul, Goldgof, and Goldgof (2020)	X-ray images	ResNet50+VGG16	135 (+)	94.40
Li et al. (2020)	CT images	COVNet	400 (+)	90.00
Zheng et al. (2020)	CT images	DeCoVNet	313 (+)	90.00
Song, Ying et al. (2020)	CT images	DRE-Net	777 (+)	86.00
Ozturk, Talo, Yildirim, Baloglu, Yildirim, and Acharya (2020)	X-ray images	DarkCovidNet	125 (+)	87.02
Khan, Shah, and Bhat (2020)	X-ray images	CoroNet	284 (+)	89.60
Wang, Kang et al. (2020)	CT images	M-Inception	195 (+)	82.90
Hassantabar, Ahmadi, and Sharifi (2020)	X-ray images	CNN	100 (+)	93.20
Shibly, Dey, Islam, and Rahman (2020)	X-ray images	VGG-16 based Fast R-CNN	183 (+)	97.36
Wang and Wong (2020)	CT images	FGCNet	320 (+)	97.71
Wang, Nayak, Guttery, Zhang and Zhang (2020)	CT images	CCSHNet	284 (+)	98.30
Zhang, Satapathy, Zhu, Górriz and Wang (2020)	CT images	7L-CNN-CD	142 (+)	94.44

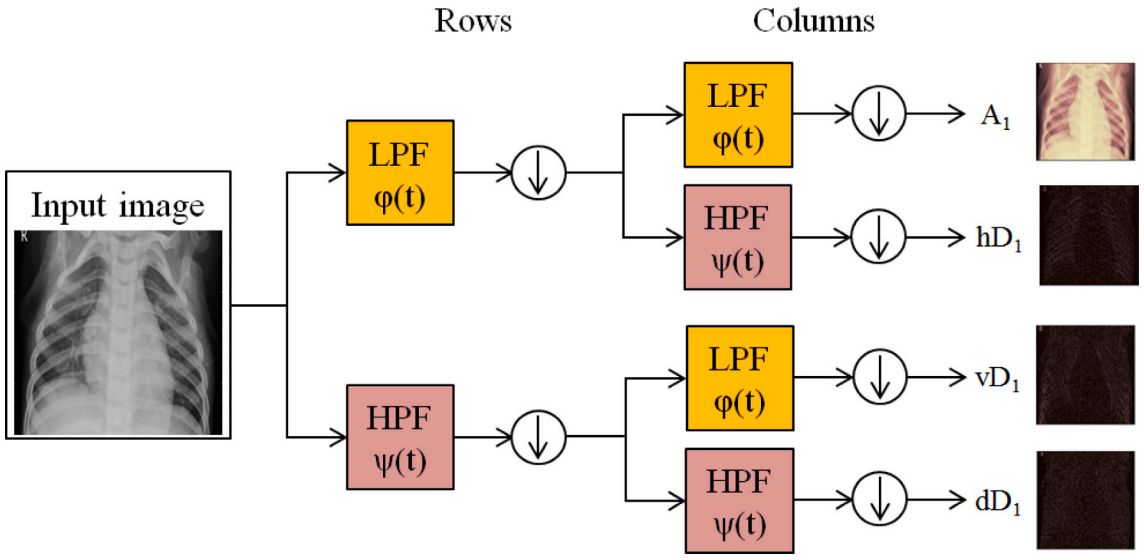

Fig. 1. Single-level decomposition through 2-D DWT.

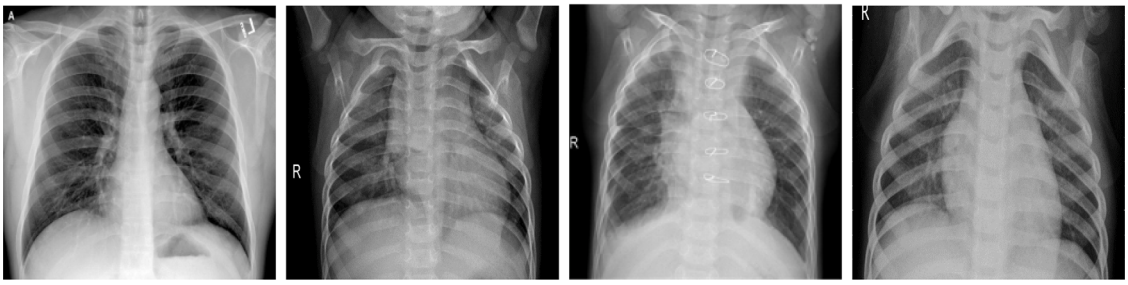

(a) COVID-19 (b) Normal (c) Pneumonia Bacterial (d) Pneumonia Viral

Fig. 2. Sample of thoracic X-ray image dataset for four-class instances.

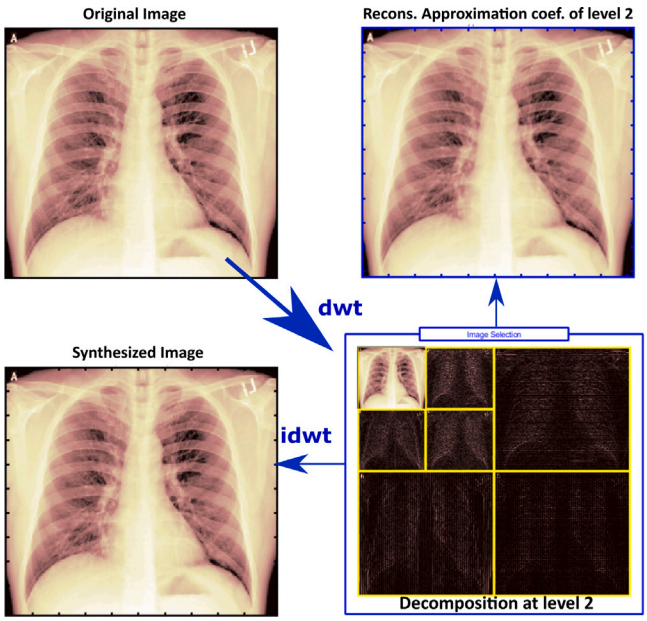

Fig. 3. Reconstructed thoracic X-ray image coefficient for db2 with DWT two-level approximation.

4. Wavelet-based deep CNN

As the next step, the collected DWT featured sub-images are channeled as input to the CNN algorithm to distinguish between the various health conditions, i.e. (COVID-19 vs. Pneumonia Viral vs. Pneumonia Bacterial vs. Normal). A deep convolution neural network architecture is based entirely on deeply separable convolution layers. A separable convolution in depth is commonly referred to as separable convolution in deep learning systems. CNN is broken down into a smaller set of layer functions. Each of these strata is a neural-network. A neural network may be either single or multi-layered. The entire workflow for network-based architecture for deep convolution neural network using DWT featured X-ray image is shown in Fig. 5. Artificial intelligence-enabled wavelet-based deep CNN takes only approximation component as input as yielded higher identification accuracy examined extensively in the discussions.

4.1. CNN model architecture and development

Most of the conventional studies used well-known network-based CNN architectures such as SqueezeNet: AlexNet (Iandola, Han, Moskewicz, Ashraf, Dally, & Keutzer, 2016), VGG-16 &VGG-19 (Sengupta, Ye, Wang, Liu, & Roy, 2019), GoogleNet (Xie et al., 2018), MobileNet-V2 (Ma, Zhang, Zheng, & Sun, 2018), ResNet-18 & ResNet-50 & ResNet-101 (Szegedy, Ioffe, Vanhoucke, & Alemi, 2016), and Xception (Chollet, 2017) and turned out that only a few models such as Xception, ResNet-50, and VGG-16 achieved better detection accuracy for SARS-nCoV from thoracic X-ray images. Thus, the proposed work used these three network-based pre-trained convolution neural-network architectures for further studies. The accuracy was enhanced using the dense layer of Keras sequential model-2 from Verma, Nagpal, Desai, and Sudha (2020) research work. A typical architecture of the convolution neural network consists of the convolution layer, the subsampling layer, and a fully connected layer. All the layers mentioned above are stacked up to form an intact architecture of the CNN. In addition to these above presented key layers, CNN includes arbitrary layers such as implementing the batch to boost training time and the dropout layer to fix the overfitting issue. The proposed deep CNN Xception-I uses Xception as a base model with a dropout layer and seven fully connected layers. One of the commonly used activation functions is softmax. Activation functions are used in the model to impart non-linearity. A neural network model can behave like a linear regression

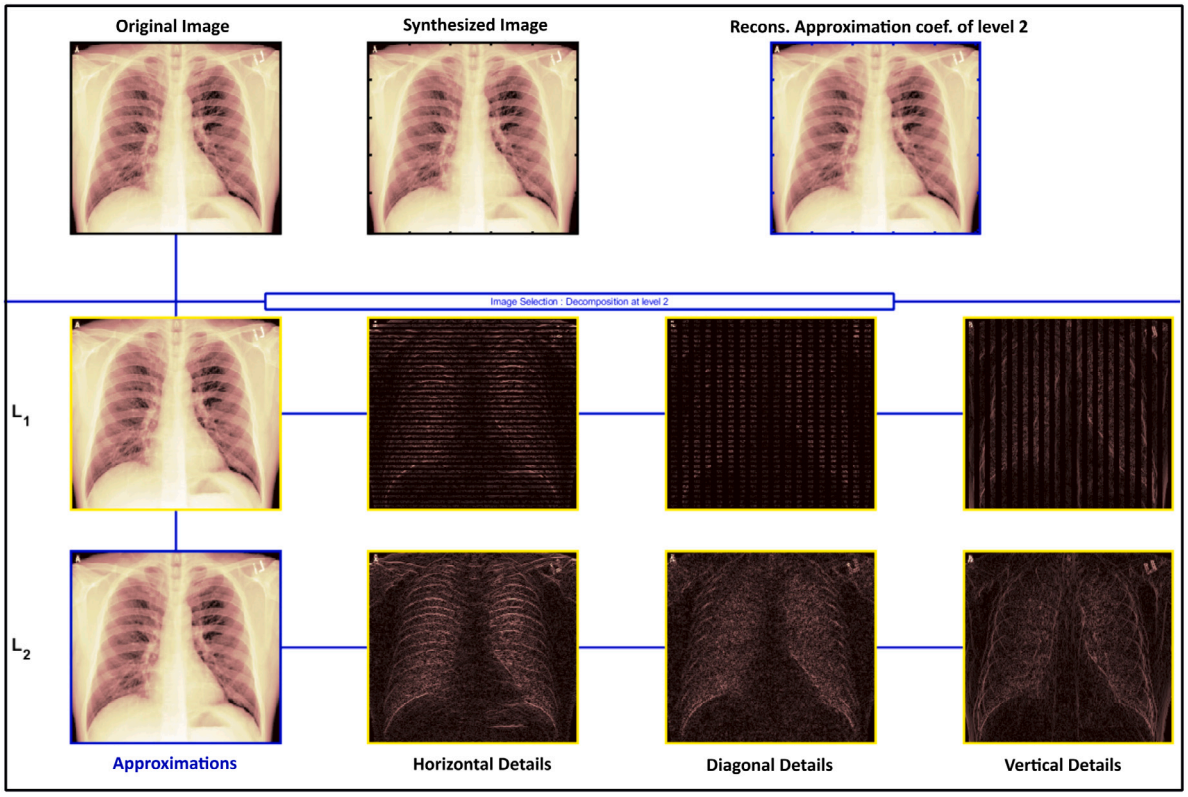

Fig. 4. Reconstructed thoracic X-ray image coefficient for db2 with DWT two-level.

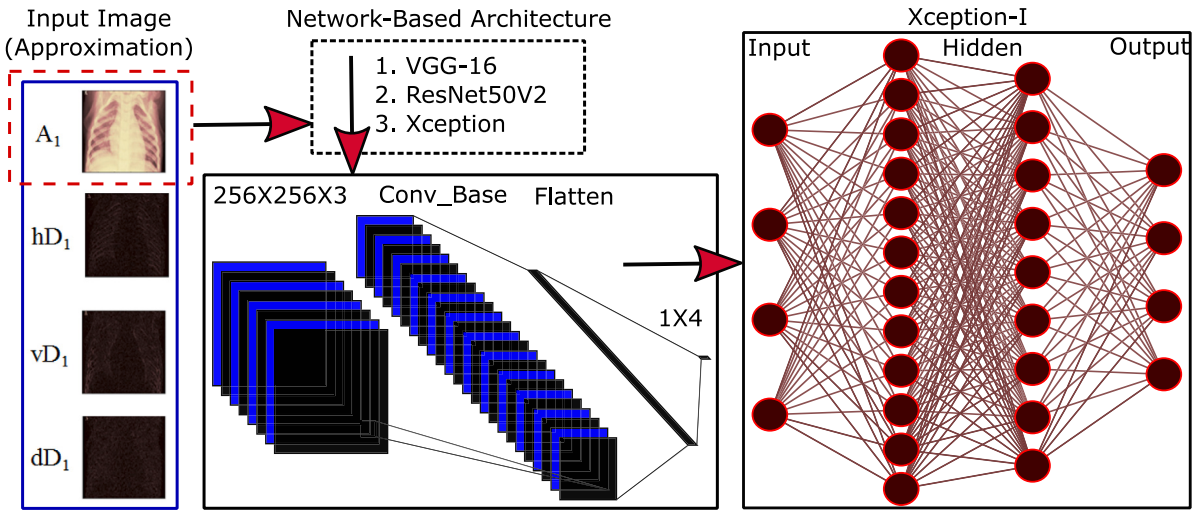

Fig. 5. Network-based architecture for deep CNN using DWT featured thoracic X-ray images.

Table 2
Image dataset description.

SN.	Disease	Number of Images
1	Normal	2398
2	Pneumonia Viral	3204
3	Pneumonia Bacterial	846
4	COVID-19	1552
	Total	**8000**

Table 3
Accuracy (in%) for various wavelets.

Wavelet	Level	
	Level1	Level2
Haar	97.25	98.35
Symlet	96.62	98.87
Biorthogonal	95.92	98.73
Coiflet	96.25	98.31
Daubechies	98.18	98.43
Discrete Meyer	93.77	96.90

model without the activation function. The softmax activation function is used in the fully connected layer for multi-label classification problem. The softmax outputs a vector representing the distributions of the probability of several possible outcomes. Xception-I has a total of 23,598,734 parameters, of which 23,544,206 are trainable, and 54,528 are non-trainable.

4.2. Training and stop learning process for CNN

The proposed wavelet-based deep convolution neural network Xception-I architecture model was implemented on top of the TensorFlow at Keras. TensorFlow is a free and open-source software library for dataflow and differentiable programming across a variety of functions. It is a symbolic math library and used for machine learning applications, such as neural networks. The image datasets collected for thoracic X-ray images are as shown in Table 2. The test data ensured that the model is not biased against the training outcomes. First, initialize weights for each layer at random, and carry out forward propagation for all input image data. The output layer error was calculated using various techniques such as RMSprop, Adam, Adamax, SGD with momentum, AdaGrad. Then a method of back-propagation was applied to adjust the weights closer to the target. The bigger the number of trainable network parameters, the greater the number of polynomials required to fit the data. The whole training phase was performed on the Google Collaboratory Ubuntu platform equipped with a Tesla K80 graphics card. The convolution neural network models were trained for different architectures with various epoch sizes, such as 40, 60, 80, 100, and 120, for learning rates of 0.0001, 1e−6 decay, batch size 10. The algorithm checks the consistency of the five-down precision to disrupt the learning process as and when progress in generalization decreases.

5. Results and discussions

This section describes in detail the implementation of the methodology described earlier and the results obtained. First, the CNN model fed the raw thoracic X-ray images without extracting any features. CNN initially analyzes the precision of three-class instances and four-class instances in detecting SARs-nCoV and extensively investigates the accuracy and loss of their identification. The proposed Xception-I architecture has performed better for four class instances than the three-class due to more image datasets. It has also extracted features from thoracic X-ray images using a discrete wavelet transformation (DWT) technique. More X-ray thoracic images and instances can contribute to the extraction of distinct features before being fed to the CNN model at the preprocessing stage. Since more information is available at the preprocessing stage, the CNN model's reliability can be improved and robust in detecting SARS-nCoV. Therefore, it used X-ray images from the wavelet to retrieve some prominent features from an X-ray and then fed them to the deep CNN model. Several wavelets have been examined with their families to determine suitability to decide which wavelets to be used to extract the feature. The test accuracy (in%) for several base wavelets with one and two levels of DWT decomposition was evaluated and described in Table 3.

Compared to single-level ones, base wavelets with two levels of decomposition were found to have performed remarkably well. Therefore, the rest of the wavelets, such as Haar, Symlet, Biorthogonal, Coiflet, Daubechies, Discrete Meyer, and their families, were evaluated on only two decomposition levels. Sym7 from Symlet (98.87%), Bior2.6 from Biorthogonal (98.73%), Coif5 from Coiflet (98.45%), DB2 from Daubechies (98.43%), Haar with two-level (98.35%), and Discrete Meyer with two-level (96.90%), wavelet families performed exceptionally well compared to the other wavelet families as listed in Table 4.

5.1. Three-class instance

Fig. 6 demonstrates the accuracy of the proposed deep convolution neural network model for three-class instances, with and without feature vectors. The figure shows the CNN model's accuracy for the epoch

Table 4
Accuracy (in%) with respect to the several wavelet families for two-levels of decomposition for DWT.

Biorthogonal (%)														
bior1.1	bior1.3	bior1.5	bior2.2	bior2.4	bior2.6	bior2.8	bior3.1	bior3.3	bior3.5	bior3.7	bior3.9	bior4.4	bior5.5	bior6.8
97.57	98.17	98.17	97.89	98.45	98.73	98.17	96.90	96.06	96.62	97.53	96.34	98.45	96.62	95.77
Daubechies (%)										Coiflet (%)				
db1	db2	db3	db4	db5	db6	db7	db8	db9	db10	coif1	coif2	coif3	coif4	coif5
98.17	98.43	97.89	97.75	95.77	96.90	97.04	96.20	98.03	96.90	97.57	98.17	98.17	97.89	98.45
Symlet (%)														
sym2		sym3		sym4		sym5		sym6		sym7		sym8		
98.59		97.89		97.46		97.89		97.89		98.87		97.04		

sizes for a Haar wavelet with one and two levels of decomposition and raw X-ray image, i.e., without any feature extraction method.

It can be concluded that the CNN model with two-level Haar decomposition has achieved greater accuracy compared to single-level DWT and raw thoracic X-ray images. The descriptive statistics of the obtained accuracy over epochs with and without wavelet for three-class instances of the Xception-I architecture are tabulated in Table 5. The maximum detection accuracy for SARS-nCoV was obtained for Haar with a two-level decomposition, i.e., 98.59%. In real-time viability, the mean and upper confidence interval (CI) of 95% for Haar with two levels of decomposition is comparatively more significant. Various performance attributes of the Xception architecture such as time per epoch and per step, training loss, training accuracy, validation loss, and validation accuracy were assessed and is shown in Table 6. Haar with two-level decomposition has taken 94 s per epoch for a total epoch size of 40 for three-class instances and has the lowest training and validation loss of 0.0290 and 0.0432, respectively.

5.2. Four-class instance

Fig. 7 demonstrates the accuracy of the proposed deep convolution neural network model for four-class instances. The figure shows the accuracy of the CNN model to the epoch sizes for a Haar wavelet with one and two decomposition levels. It can be concluded that irrespective of the class instances, the CNN model with two-level Haar decomposition has achieved greater accuracy than single-level DWT. Similarly, descriptive statistics of the obtained accuracy over epochs with Haar wavelet for four-class instances and their explicit performance attributes of the Xception-I architecture are tabulated in Tables 7 and 8, respectively.

5.3. Accuracy over epoch size

Fig. 8 shows the accuracy of the proposed CNN model for four-class instances concerning different epoch sizes for a Haar wavelet with one and two decomposition levels. From Tables 9 and 10, it was observed that the proposed CNN architecture, Xception-I has a relatively low standard error (SE) of mean and standard deviation for an epoch size of 40. Also, the time per epoch is 109 s, with a validity loss of 0.0576. The accuracy of the proposed Xception-I with a 40 epoch size may be an optimal option, as it takes less time to provide less validity loss than other epoch sizes. The proposed wavelet-based deep convolution neural network architectures for various wavelets and their families were run with 40 epochs for learning rates of 0.0001, 1e−6 decay, and batch size 10.

5.4. Accuracy over wavelet component

Discrete Wavelet Transforms (DWT) implements a combination of low-pass $\phi(t)$ and high-pass $\psi(t)$ filters to achieve the approximation and detail wavelet coefficients, respectively, by downsampling the input image. The approximation coefficients are the essential sub-band and include the low-frequency and high-scale input signal components. In contrast, the detail coefficients have high-frequency and low-scale component details, such as the input image's noise (Farghaly et al. 2020). CNN fed with wavelet featuring approximation component of thoracic X-ray images was found to have outperformed detailed components and provided much higher accuracy of SARS-nCoV detection. Table 11, the performance comparison of Xception-I over wavelet components for four-class instances is listed. One of the fascinating key findings of the proposed work to use only the wavelet approximation component for any further study of thoracic X-ray images.

5.5. Network-based architecture

First, the performance comparison attributes of network-based pre-trained deep CNN architectures, ResNet50V2, VGG16, Xception, were evaluated in Table 12. It was observed that among the three architectures compared, Xception had performed well. Although VGG16 takes less test time and the number of SARS-nCoV detection parameters in the CNN architecture, the detection accuracy has diminished significantly compared to other architectures. The proposed Xception-I architecture further improved detection accuracy using hyper-tuning parameters, hitting 98.35%. Xception-I architecture has 23.59 M parameters, with an appropriate training and validation loss of 0.0483 and 0.0576. Fig. 9 shows the accuracy and loss plots for different CNN architectures over 40 epoch runs. ResNet50V2 architecture trained the CNN model well enough, but it failed on the validation part. The training and validation performed well with other architectures with minor improvements in the accuracy of SARS-nCoV detection.

6. Experimental validation

Cross-validation is a statistical method used in this analysis to approximate the abilities of proposed deep learning to assess knowledge on new or unseen data. The procedure has a parameter, k, which refers to the k-fold Cross-Validation method. The proposed wavelet-based deep learning models were for both two-class (COVID vs. non-COVID) and four-class (COVID vs. non-COVID vs. Bacterial Pneumonia vs. Viral Pneumonia) cases validated using publicly available databases Kaggle (Tabik et al., 2020) and Github (Khan et al., 2020). Rodriguez et al. presented sensitivity analysis of k-Fold cross-validation in prediction error estimation. Rodriguez, Perez, and Lozano (2009) suggested k = 5 or k = 10 folds produce the lowest error since they are less biased than any other k-Fold CV technique.

Initially, k = 1 to 10 was used to assess the results in this study. Later, for any further analysis, 5 and 10 fold CV were used on two-class and four-class instances since they induce minor error and are less biased than any other k-Fold CV. The machine learning model was then validated with unseen data sets from public datasets, such as Kaggle and Github, with 5 and 10 fold in order to measure its robustness. From the literature, the sensitivity of thoracic X-ray images was higher than that of rRT-PCR and discussed extensively in the introduction section. The low sensitivity of PCR could be because of the low efficiency of viral nucleic acid detection, including the immature development of nucleic acid detection technology, the variability

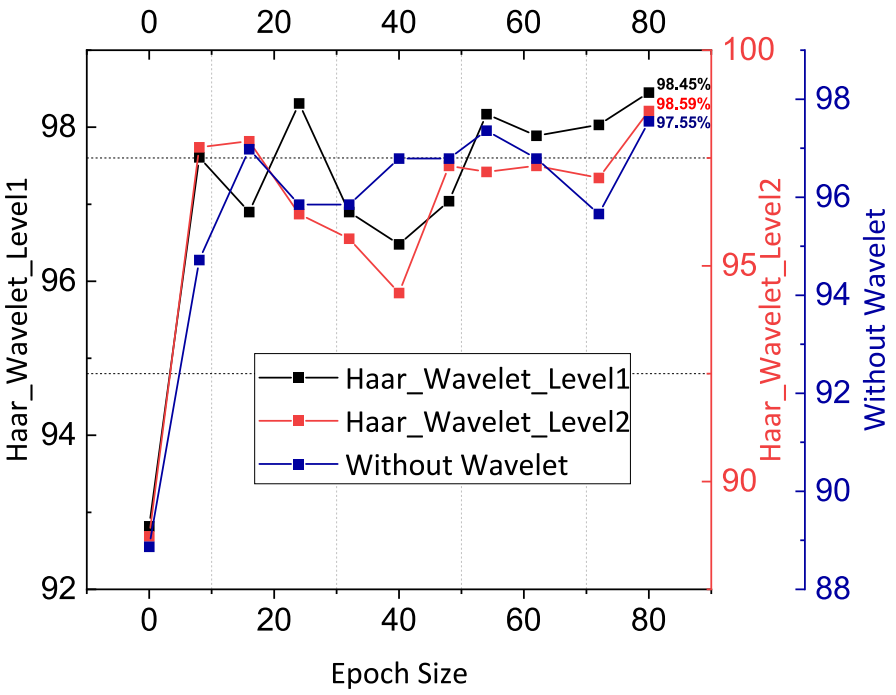

Fig. 6. Accuracy with and without wavelet for three-class instances.

Table 5
Descriptive statistics of the accuracy with and without wavelet for three-class instances.

Descriptive Statistics	Mean	Standard Deviation	SE of mean	Lower 95% CI of Mean	Upper 95% CI of Mean	Min	Median	Max
Haar_Wavelet_Level1	97.14	1.57	0.47	96.08	98.20	92.82	97.61	98.45
Haar_Wavelet_Level2	98.18	2.73	0.82	94.34	98.01	88.73	97.18	98.59
Without Wavelet	95.74	2.42	0.73	94.11	97.37	88.87	96.79	97.55

Table 6
Performance comparison of Xception-I with and without wavelet for three-class instances.

Model (Xception-I)	Time Taken Per Epoch	Time Taken Per Step	Training Loss	Training Accuracy	Validation Loss	Validation Accuracy
Haar_Wavelet_Level1	173 s	605 ms	0.0651	0.9776	0.0567	0.9845
Haar_Wavelet_Level2	94 s	330 ms	0.0290	0.9912	0.0432	0.9859
Without Wavelet	89 s	412 ms	0.0316	0.9888	0.0822	0.9755

Table 7
Descriptive statistics of DWT featured thoracic X-ray images for four-class instances.

Descriptive Statistics	Mean	Standard Deviation	SE of mean	Lower 95% CI of Mean	Upper 95% CI of Mean	Min	Median	Max
Haar_Wavelet_Level1	94.87	1.02	0.30	94.19	95.56	92.62	95.00	96.63
Haar_Wavelet_Level2	96.57	0.99	0.29	95.90	97.24	94.81	96.96	97.85
Haar_Wavelet_Level1, 2	96.09	1.40	0.42	95.14	97.03	93.46	96.54	97.74

Table 8
Performance comparison of Xception-I for DWT featured thoracic X-ray images for four-class instances.

Model (Xception-I)	Time Taken Per Epoch	Time Taken Per Step	Training Loss	Training Accuracy	Validation Loss	Validation Accuracy
Haar_Wavelet_Level1	120 s	375 ms	0.1087	0.9604	0.1030	0.9663
Haar_Wavelet_Level2	105 s	330 ms	0.0414	0.9865	0.1216	0.9785
Haar_Wavelet_Level1, 2	400 s	625 ms	0.0454	0.9856	0.0706	0.9774

Table 9
Descriptive statistics of the accuracy in different epoch sizes for four-class instances.

Epochs /Descriptive Statistics	Mean	Standard Deviation	SE of mean	Lower 95% CI of Mean	Upper 95% CI of Mean	Min	Median	Max
Accuracy_20epoch	96.08	1.05	0.3179	95.37	96.79	94.05	96.33	97.34
Accuracy_40epoch	97.44	0.65	0.1969	97.00	97.88	96.08	97.34	98.35
Accuracy_60epoch	96.38	1.72	0.5190	95.23	97.54	92.53	96.84	98.61
Accuracy_80epoch	97.37	0.89	0.2704	96.77	97.97	95.82	97.72	98.48
Accuracy_100epoch	97.64	0.63	0.1904	97.21	98.06	96.58	97.85	98.61

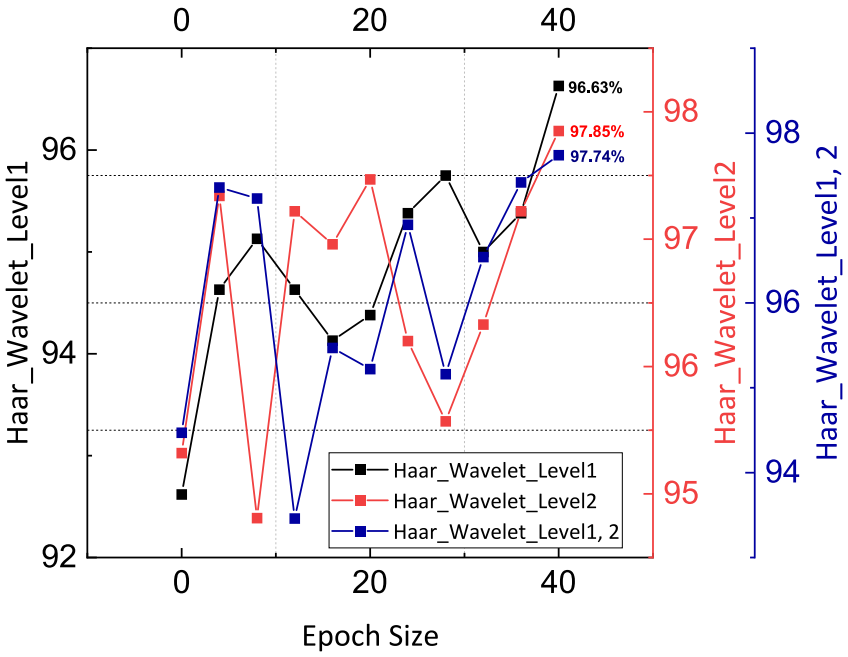

Fig. 7. Xception-I demonstrates accuracy of DWT featured thoracic X-ray images for four-class instances.

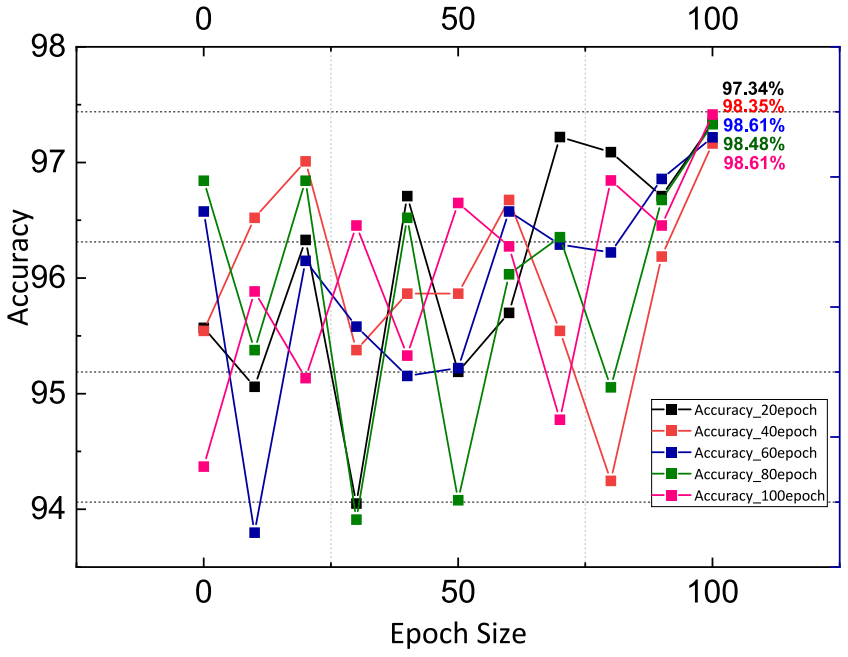

Fig. 8. Xception-I demonstrates accuracy concerning different epoch sizes for four-class instances.

Table 10
Performance comparison of Xception-I for four-class instances over different epoch sizes.

Model (Xception-I)	Time Taken Per Epoch	Time Taken Per Step	Training Loss	Training Accuracy	Validation Loss	Validation Accuracy
Accuracy_20epochs	203 s	633 ms	0.0967	0.9699	0.1240	0.9734
Accuracy_40epochs	109 s	342 ms	0.0483	0.9856	0.0576	0.9835
Accuracy_60epochs	110 s	341 ms	0.0808	0.9731	0.0508	0.9861
Accuracy_80epochs	103 s	322 ms	0.0425	0.9884	0.0694	0.9848
Accuracy_100epochs	195 s	610 ms	0.0341	0.9912	0.0604	0.9861

of the detection rate from different manufacturers, low patient viral load, or insufficient clinical sampling, etc. In Table 13, the average class-wise precision, recall, dice similarity coefficient (DSC) of the proposed deep learning model is presented to examine the sensitivity of the proposed wavelet-based technology for the COVID-19 testing procedure.

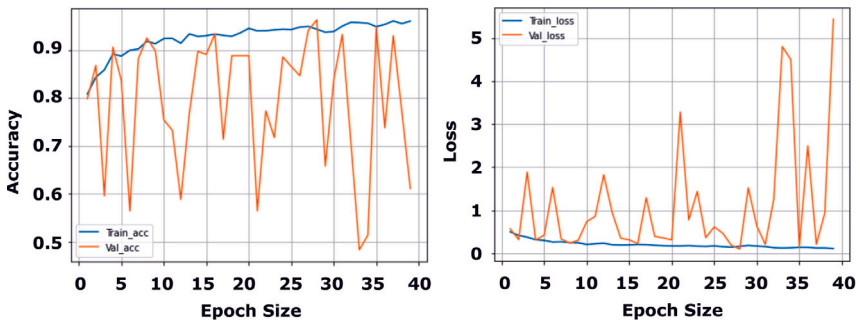

(a) ResNet50V2.

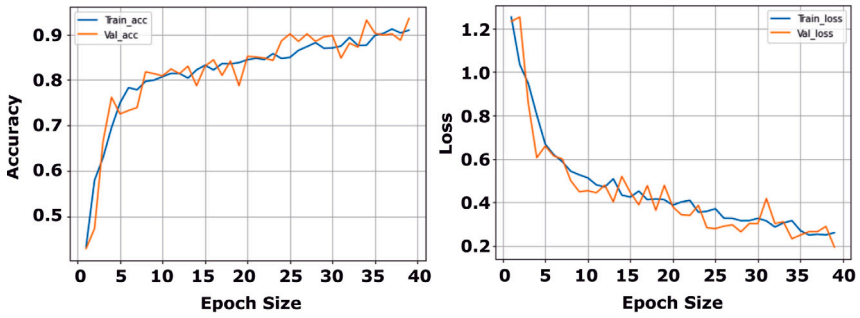

(b) VGG16.

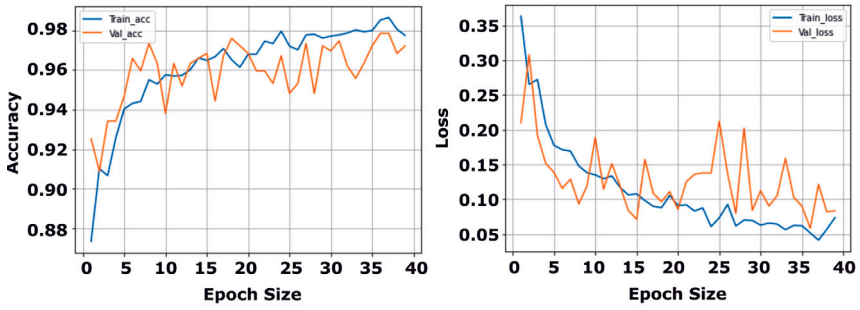

(c) Xception.

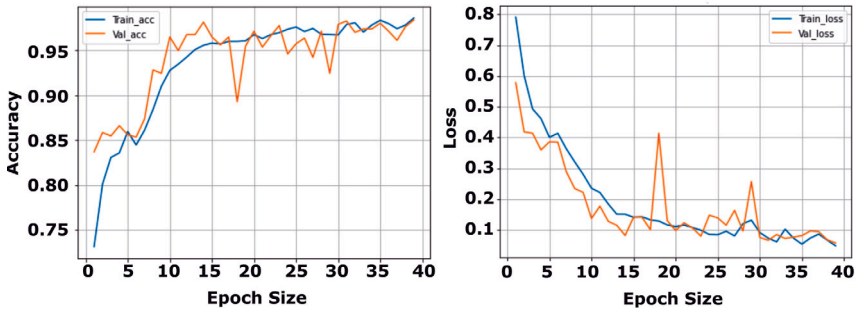

(d) Xception-I.

Fig. 9. The accuracy and loss plots for different CNN architectures.

To investigate the heterogeneity and robustness of deep learning models, the proposed xception-I was tested on both two-class and four-class instances from Kaggle and Github datasets. The 5-fold and 10-fold CV strategies are thoroughly examined in Sections 6.1 and 6.2.

6.1. Two-class instances

For the cross-validation techniques, 2344 thoracic X-ray images that were fed to the model belongs to two-class instances (COVID vs. Non-COVID) and observed to misclassify only 46 images on 5-Fold CV and

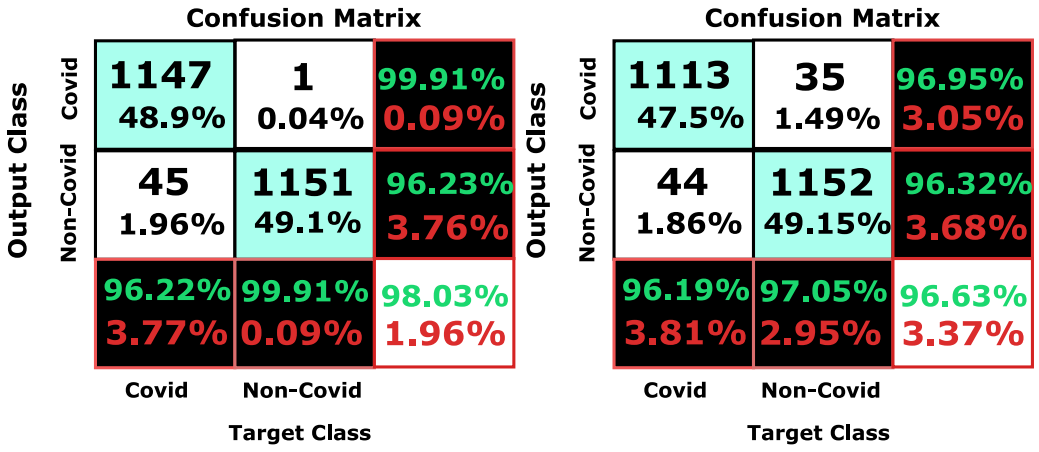

(a) 5 fold CV from Kaggle on 2344 dataset. (b) 10 fold CV from Kaggle on 2344 dataset.

Fig. 10. Confusion matrix for two-class instances with 5 and 10 fold CV.

Table 11
Performance comparison of Xception-I for four-class instances over wavelet components.

Wavelet Component		Time Taken Per Epoch	Training Loss	Training Accuracy	Validation Loss	Validation Accuracy
Detail	Diagonal	95 s	1.0456	0.5408	1.0341	0.5535
	Vertical	94 s	0.7551	0.6948	0.6773	0.7514
	Horizontal	98 s	0.6917	0.7289	0.6459	0.7634
Approximation		188 s	0.0803	0.9740	0.0507	0.9887

Table 12
Performance comparison of network-based pre-trained architectures.

Model	Time Taken Per Epoch	Time Taken Per Step	Training Loss	Training Accuracy	Validation Loss	Validation Accuracy	Params (in M)
ResNet50V2	125 s	393 ms	0.1701	0.9390	0.6384	0.8392	36.22
VGG16	84 s	265 ms	0.2609	0.9095	0.1941	0.9354	16.81
Xception	106 s	332 ms	0.0517	0.9852	0.0585	0.9785	36.62
Xception-I	109 s	342 ms	0.0483	0.9856	0.0576	0.9835	23.59

Table 13
Average class-wise precision, recall, DSC for four-class instances.

Class	Precision	Recall	DSC
Pneumonia Bacterial (PNA Bact.)	0.98	0.93	0.97
COVID-19	0.99	0.98	0.99
Normal	0.99	0.97	0.98
Pneumonia Viral (PNA Viral)	0.96	1.00	0.98

Table 14
Evaluation assessment of Xception-I on each fold.

Folds	Precision	Recall	DSC	Accuracy	Support
fold1	0.98	0.98	0.98	0.9800	400 X-ray
fold2	0.97	0.96	0.98	0.9700	400 X-ray
fold3	0.98	0.99	0.98	0.9850	400 X-ray
fold4	0.97	0.97	0.97	0.9725	400 X-ray
fold5	0.99	0.99	0.99	0.9825	400 X-ray
fold10	0.98	1.00	1.00	0.9950	400 X-ray
Weighted Average	97.83	98.16	98.33	98.080	

79 on 10-Fold CV with a minimal test loss of 0.0926 and 0.0465 respectively. Fig. 10 shows the confusion matrix for two-class instances with 5 and 10 fold cross validation.

6.2. Four-class instances

The proposed wavelet-based deep learning xception-I model has performed remarkably well on the unseen data from different databases such as Kaggle and Github. For the cross-validation, the first 400 thoracic X-ray images were fed to the model, 393 images were correctly classified, and seven were classified as normal on a 5-fold CV. Similarly, 10-fold CV techniques were applied on the same data and observed to have only 2 misclassified images as pneumonia viral. The proposed method has also been validated on a 1004 image dataset and observed to have only 20 misclassified images. The normalized confusion matrix plot of the predictions set for validity is shown in Fig. 11.

The Xception-I model has predicted COVID-19 and PNA Viral groups with slightly higher precision than other groups, as seen from the confusion matrix. Since these instances have been imbalanced, one hypothesis is to produce more images with data augmentation for the cases with less data than the others and achieve approximately the same number of images. The evaluation assessment of the proposed CNN architecture Xception-I on each fold is listed in Table 14. The estimated error from each k-folds cross validation procedure is shown in Fig. 12. When compared to other folds, 10-Fold CV has the lowest error rate and the highest COVID-19 identification accuracy. In addition, the performance comparison of the proposed convolution neural network (CNN) architecture Xception-I has been compared with other literature methods.

Numerous methods have been developed to identify the novel 2019 coronavirus disease, but only a few techniques have more than 95% identification accuracy, as listed in Table 15. However, some approaches have focused on two-class (COVID vs. non-COVID) or three-class (COVID vs. non-COVID vs. Pneumonia) instances with fewer thoracic X-ray image datasets. Only a few models were performed on

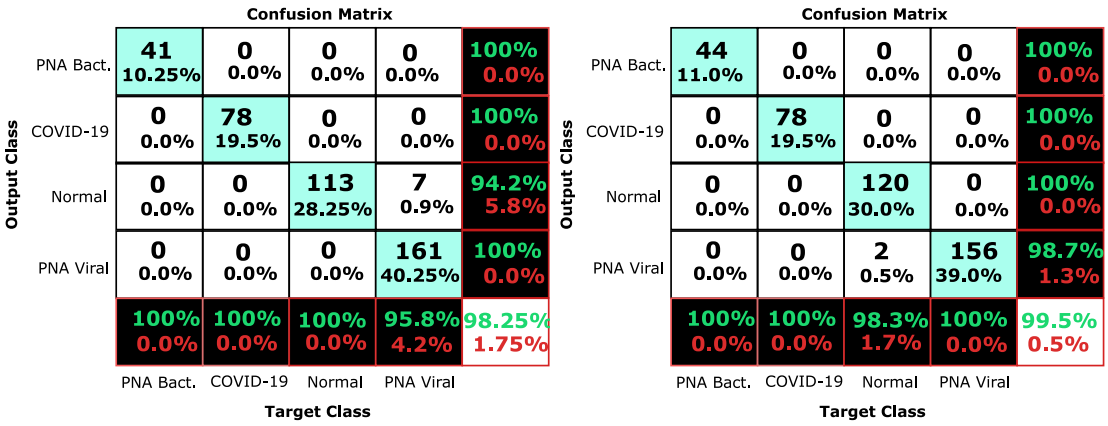

(a) 5 fold CV from Github on 400 dataset. (b) 10 fold CV from Github on 400 dataset.

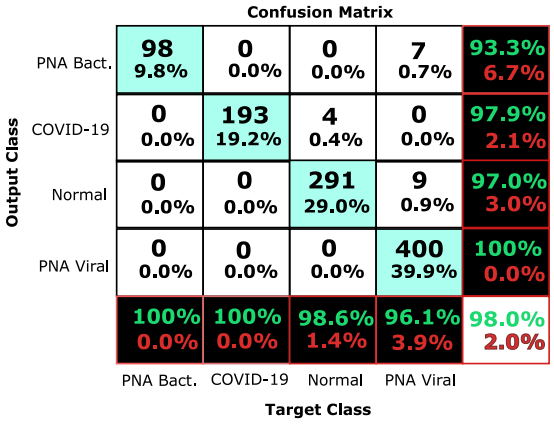

(c) 5 fold CV from Github on 1004 dataset.

Fig. 11. Confusion matrix for four-class instances with 5 and 10 fold CV.

four class instances (COVID vs. non-COVID vs. Bacterial Pneumonia vs. Viral Pneumonia). Thus, the proposed study contributes in a novel way to improved identification accuracy in a large number of image datasets.

A few thoracic X-ray images were not correctly aligned as shown in Fig. 13, causing the CNN network to learn different features than typical datasets, resulting in a lower classification accuracy. In this study, these misaligned datasets were manually excluded before feeding them to the CNN model. A person suffering from COVID-19 with asymptomatic symptoms may or may not have infected lungs, which may be misclassified as normal or bacterial or viral pneumonia. In this investigation, only the development of illness from bacterial or viral pneumonia to COVID-19 was examined. The severity analysis of persons who are with asymptomatic and COVID-19 and its progression can be studied provided datasets are available for the same. Also, a person with COVID-19 symptoms and pneumonia (mild, moderate, or severe) may have distinct X-ray scans, which were not considered in this study.

7. Managerial implications

The primary purpose of sensitivity analysis is to determine management implications and insights (Gharaei, Hoseini Shekarabi, Karimi, Pourjavad & Amjadian, 2019). According to optimality criteria such as the number of iterations, optimality error, infeasibility, and complementarity, the suggested technique performed exceptionally well. There are extensive reviews of alternative sensitivity analysis solution approaches that use a similar optimality criterion (Awasthi & Omrani, 2019; Gharaei, Hoseini Shekarabi & Karimi, 2020; Gharaei, Karimi & Hoseini Shekarabi, 2020; Gharaei, Karimi & Shekarabi, 2019; Giri & Masanta, 2020; Rabbani, Hosseini-Mokhallesun, Ordibazar, &

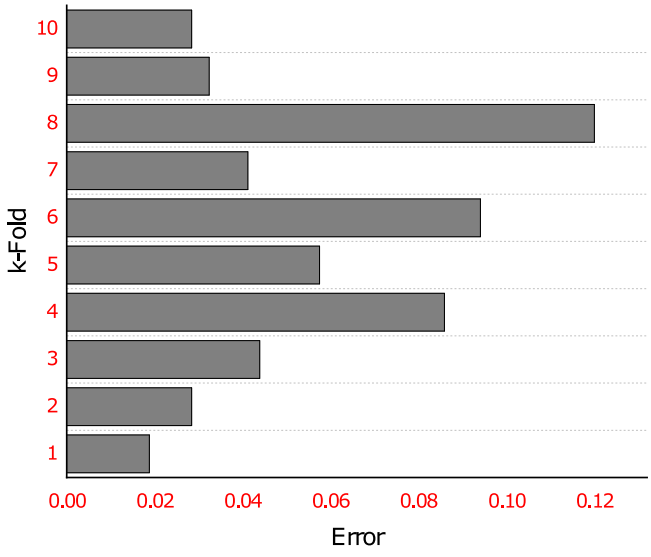

Fig. 12. Error estimation with respect to the k-Fold CV.

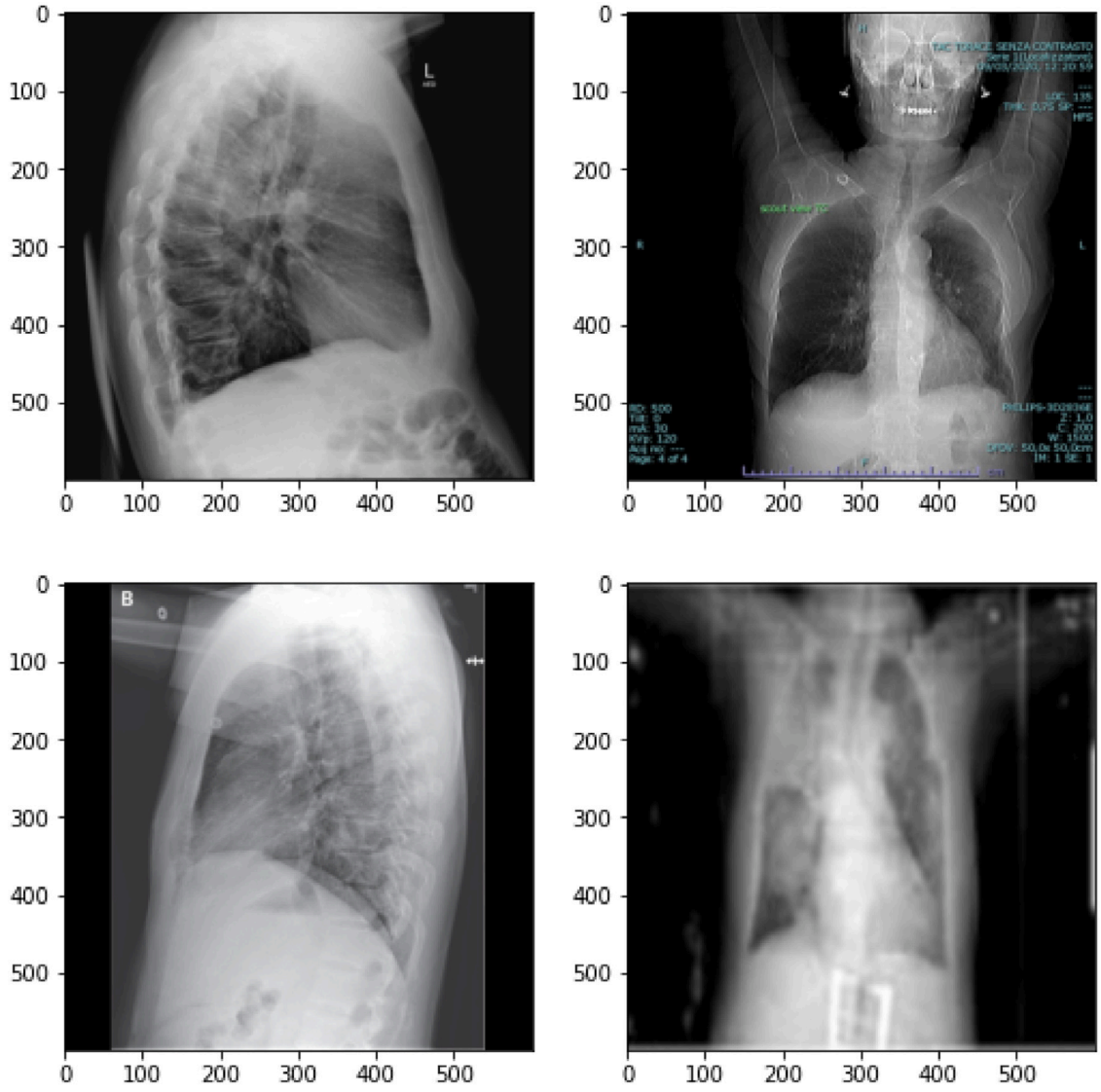

Fig. 13. Misaligned thoracic X-ray images from collected dataset.

Table 15
Performance comparison of CNN architecture Xception-I from literature.

Authors	Image modality	Method used	COVID-19 cases	Acc (%)
Xu et al.	CT images	ResNet-18 + location attention	219 (+)	86.70
Zhang et al.	X-ray images	ResNet-18 + classification head + anomaly detection head	100 (+)	96.00
Wang et al.	X-ray images	COVID-Net	53 (+)	92.40
Sethy et al.	X-ray images	ResNet50+SVM	25 (+)	95.38
Wang et al.	CT images	DenseNet121	924 (+)	80.12
Narin et al.	X-ray images	Deep CNN ResNet-50	50 (+)	98.00
Gozes et al.	CT images	ResNet-50	50 (+)	94.00
Apostolopoulos et al.	X-ray images	VGG-19	244 (+)	93.48
Hemdan et al.	X-ray images	COVIDX-Net	25 (+)	90.00
Abbas et al.	X-ray images	DeTrac	105 (+)	95.12
Hall et al.	X-ray images	ResNet50+VGG16	135 (+)	94.40
Li et al.	CT images	COVNet	400 (+)	90.00
Zheng et al.	CT images	DeCoVNet	313 (+)	90.00
Song et al.	CT images	DRE-Net	777 (+)	86.00
Ozturk et al.	X-ray images	DarkCovidNet	125 (+)	87.02
Khan et al.	X-ray images	CoroNet	284 (+)	89.60
Wang et al.	CT images	M-Inception	195 (+)	82.90
Hassantabar et al.	X-ray images	CNN	100 (+)	93.20
Shibly et al.	X-ray images	VGG-16 based Fast R-CNN	183 (+)	97.36
Proposed work	**X-ray images**	**Wavelet based Deep CNN**	**1552 (+)**	**98.87**

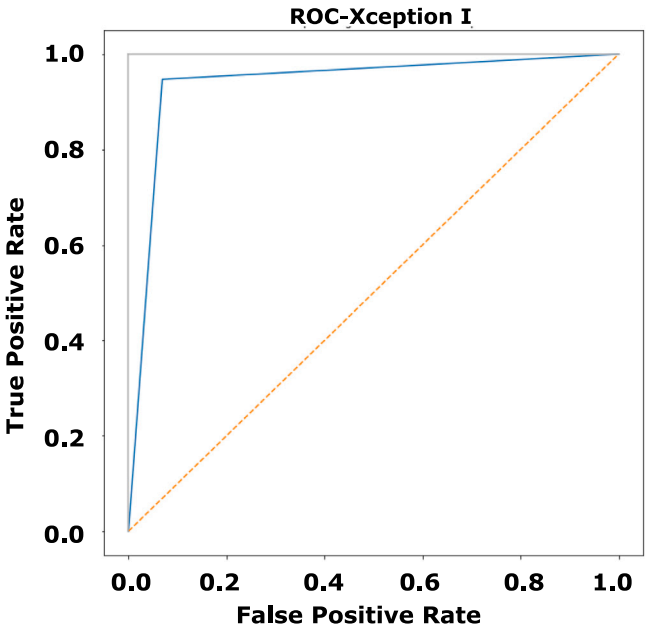

Fig. 14. Error estimation with respect to the k-Fold CV.

Farrokhi-Asl, 2020; Tsao, 2015). The proposed algorithm is used to select the optimal error based on the number of iterations in the proposed architectures, the optimizer for loss calculation, the number of epoch sizes, learning rates, and batch sizes. Furthermore, the proposed technique examines five-down precision to disrupt the learning process when generalization progress decreases. Complementarity gives match quality through differences—capabilities are complementary if they are different in a way that can be combined to create greater value (Mitsuhashi & Greve, 2009). Complementarity simulate negative externalities, in which the relative payoff of one activity drops as the number of agents playing it grows (Bramoullé, 2001). The proposed algorithm investigated complementarity and infeasibility by changing the number of epoch runs, k-fold for CV methods, and analyzing the change in COVID-19 detection accuracy (ref. Section 6). According to optimality criteria such as iterations, infeasibility, optimal error, and complementarity, the proposed method performed exceptionally well. Receiver Operating Characteristic (ROC) curve analysis was used to study the diagnostic performance of RT-PCR. However, it offers very low sensitivity, 60%–70% (Hasab, 2020). In addition, all of the essential parameters were subjected to sensitivity analysis in order to determine the impact of parameter modifications. The ROC curve for the proposed method on considering optimality criterion parameters is shown in Fig. 14. Based on the sensitivity analysis, we provided various management implications and insights to assist radiologist in their decision-making process for any further clinical analysis.

8. Conclusion

In this investigation, a wavelet and the artificial intelligence-enabled testing protocol was developed for patients with SARS-nCoV through deep learning from DWT featuring thoracic X-ray images. The suggested technology, which includes DWT into the CNN model with thoracic X-ray images, outperformed CT scans and offered much greater SARS-nCoV detection accuracy. The proposed CNN architectural model tested some images on CT scans and found identical, compelling results. Most studies either worked on a small dataset or considered two (COVID-19 vs. Normal) or three-class instances (COVID-19 vs. Influenza-A-viral/Pneumonia vs. Normal) and achieved less accurate identification SARS-nCoV compared to the research work being proposed. Thus, the proposed work contributes in a novel way to detecting SARS-nCoV on a broad set of DWT featured X-ray images for a four-class instance (COVID-19 vs. Pneumonia Viral vs. Pneumonia Bacterial vs. Normal). Various performance attributes of the CNN architecture, such as time taken per epoch, time taken per step, training loss, training accuracy, validation loss, and validation accuracy, were assessed. In conclusion, the two-level Symlet 7 approximation components had the most significant test accuracy (98.87%), followed by Biorthogonal 2.6 (98.73%). Although Symlet 7 and Biorthogonal 2.6 test accuracy is outstanding, Haar and Daubechies' k-fold cross-validation accuracy scored significantly better on unseen data using a two-level DWT. For the two-class case (COVID vs. Non-COVID), 2344 thoracic X-ray images were fed into the model. With a minimal test loss of 0.0926 and 0.0465, the model misclassified 46 images on a 5-Fold CV and 79 images on a 10-Fold CV. The following 400 thoracic X-ray images were fed into the model on a 5-fold CV, with 393 being correctly classified and seven being identified as normal in the four-class instance. Only two misclassified images as pneumonia viral were detected using 10-fold CV techniques on the same data. Besides, the proposed method was evaluated on a 1004 large image dataset, with just 20 misclassified images reported. A few limitations with collected datasets might have been the rationale for these misclassified images. In particular, with the proposed architectural models for four-class instances (COVID-19 vs. Bacterial Pneumonia vs. Viral Pneumonia vs. Normal), the precision, recall rate, and dice similarity coefficient (DSC) for COVID-19 are 98%, 98%, and 99% respectively.

Table 16
Xception architecture.

Layer (Type)	Output Shape	Param #
Xception (Model)	(None, 5, 5, 2048)	20861480
flatten_1 (Flatten)	(None, 51200)	0
dropout_1 (Dropout)	(None, 51200)	0
dense_2 (Dense)	(None, 256)	15360300
dense_3 (Dense)	(None, 4)	1204
Total params: 36,222,984		
Trainable params: 36,168,456		
Non-trainable params: 54,528		

Table 17
VGG-16 architecture.

Layer (Type)	Output Shape	Param #
vgg16 (Model)	(None, 4, 4, 512)	14714688
flatten_1 (Flatten)	(None, 51200)	0
dropout_1 (Dropout)	(None, 51200)	0
dense_2 (Dense)	(None, 256)	15360300
dense_3 (Dense)	(None, 4)	1204
Total params: 16,813,124		
Trainable params: 16,813,124		
Non-trainable params: 0		

Table 18
Inception_ResNet50V2 architecture.

Layer (Type)	Output Shape	Param #
resnet50v2 (Model)	(None, 5, 5, 2048)	23564800
flatten_1 (Flatten)	(None, 51200)	0
dropout_1 (Dropout)	(None, 51200)	0
dense_2 (Dense)	(None, 256)	15360300
dense_3 (Dense)	(None, 4)	1204
Total params: 36,673,284		
Trainable params: 36,627,844		
Non-trainable params: 45,440		

Source code and dataset

The data and codes of the proposed wavelet technology will be made accessible upon publication and will be openly accessible. The proposed study has used some of the datasets of recent COVID-19

Table 19
Wavelet-featured deep CNN Xception-I architecture.

Layer (Type)	Output Shape	Param #
Xception (Model)	(None, 5, 5, 2048)	20861480
flatten_1 (Flatten)	(None, 51200)	0
dropout_1 (Dropout)	(None, 51200)	0
dense (Dense)	(None, 50)	2560050
dense_1 (Dense)	(None, 100)	5100
dense_2 (Dense)	(None, 150)	15150
dense_3 (Dense)	(None, 200)	30200
dense_4 (Dense)	(None, 250)	50250
dense_5 (Dense)	(None, 300)	75300
dense_6 (Dense)	(None, 4)	1204
Total params: 23,598,734		
Trainable params: 23,544,206		
Non-trainable params: 54,528		

patients collected from radiologists to assess the efficiency of the presented wavelet technology and examine the real-time viability of addressing the present pandemic situation in quick and efficient testing. https://github.com/prerna1694/CoVDet.git

CRediT authorship contribution statement

Amar Kumar Verma: Conceptualization, Data curation, Writing – original draft, Investigation, Software. **Inturi Vamsi:** Methodology. **Prerna Saurabh:** Data curation, Validation, Investigation. **Radhika Sudha:** Supervision, Reviewing and Editing, Data curation. **Sabareesh G.R.:** Supervision, Reviewing and editing. **Rajkumar S.:** Supervision, Introduction and literature survey.

Declaration of competing interest

The authors declare that they have no known competing financial interests or personal relationships that could have appeared to influence the work reported in this paper.

Appendix. Descriptions of the proposed CNN architectures

See Tables 16–19.

References

Abbas, A., Abdelsamea, M. M., & Gaber, M. M. (2020). Classification of COVID-19 in chest X-ray images using DeTraC deep convolutional neural network. arXiv preprint arXiv:2003.13815.

Apostolopoulos, I. D., & Mpesiana, T. A. (2020). Covid-19: automatic detection from x-ray images utilizing transfer learning with convolutional neural networks. *Physical and Engineering Sciences in Medicine*, 1.

Awasthi, A., & Omrani, H. (2019). A goal-oriented approach based on fuzzy axiomatic design for sustainable mobility project selection. *International Journal of Systems Science: Operations & Logistics*, *6*(1), 86–98.

Balavignesh, V., Gundepudi, B., Sabareesh, G., & Vamsi, I. (2018). Comparison of conventional method of fault determination with data-driven approach for ball bearings in a wind turbine gearbox. *International Journal of Performability Engineering*, *14*(3), 397–412.

Barstugan, M., Ozkaya, U., & Ozturk, S. (2020). Coronavirus (covid-19) classification using ct images by machine learning methods. arXiv preprint arXiv:2003.09424.

Bramoullé, Y. (2001). Complementarity and social networks. Available at SSRN 1028335.

Bressem, K. K., Adams, L., Erxleben, C., Hamm, B., Niehues, S., & Vahldiek, J. (2020). Comparing different deep learning architectures for classification of chest radiographs. arXiv preprint arXiv:2002.08991.

Catanzaro, M., Fagiani, F., Racchi, M., Corsini, E., Govoni, S., & Lanni, C. (2020). Immune response in COVID-19: addressing a pharmacological challenge by targeting pathways triggered by SARS-CoV-2. *Signal Transduction and Targeted Therapy*, *5*(1), 1–10.

Celik, Y., Talo, M., Yildirim, O., Karabatak, M., & Acharya, U. R. (2020). Automated invasive ductal carcinoma detection based using deep transfer learning with whole-slide images. *Pattern Recognition Letters*.

Chakraborty, J., & Nandy, A. (2020). Discrete wavelet transform based data representation in deep neural network for gait abnormality detection. *Biomedical Signal Processing and Control*, *62*, Article 102076.

Chaudhary, P. K., & Pachori, R. B. (2021). FBSED based automatic diagnosis of COVID-19 using X-ray and CT images. *Computers in Biology and Medicine*, Article 104454.

Chollet, F. (2017). Xception: Deep learning with depthwise separable convolutions. In *Proceedings of the IEEE conference on computer vision and pattern recognition* (pp. 1251–1258).

Chung, M., Bernheim, A., Mei, X., Zhang, N., Huang, M., Zeng, X., et al. (2020). CT imaging features of 2019 novel coronavirus (2019-nCoV). *Radiology*, *295*(1), 202–207.

Codella, N. C., Nguyen, Q.-B., Pankanti, S., Gutman, D. A., Helba, B., Halpern, A. C., et al. (2017). Deep learning ensembles for melanoma recognition in dermoscopy images. *IBM Journal of Research and Development*, *61*(4/5), 5–1.

Corman, V. M., Landt, O., Kaiser, M., Molenkamp, R., Meijer, A., Chu, D. K., et al. (2020). Detection of 2019 novel coronavirus (2019-nCoV) by real-time RT-PCR. *Eurosurveillance*, *25*(3), Article 2000045.

Cruz-Roa, A., Basavanhally, A., González, F., Gilmore, H., Feldman, M., Ganesan, S., et al. (2014). Automatic detection of invasive ductal carcinoma in whole slide images with convolutional neural networks. In *Medical imaging 2014: Digital pathology, vol. 9041*. International Society for Optics and Photonics, Article 904103.

Esteva, A., Kuprel, B., Novoa, R. A., Ko, J., Swetter, S. M., Blau, H. M., et al. (2017). Dermatologist-level classification of skin cancer with deep neural networks. *Nature*, *542*(7639), 115–118.

Fang, Y., Zhang, H., Xie, J., Lin, M., Ying, L., Pang, P., et al. (2020). Sensitivity of chest CT for COVID-19: comparison to RT-PCR. *Radiology*, Article 200432.

Gaál, G., Maga, B., & Lukács, A. (2020). Attention u-net based adversarial architectures for chest x-ray lung segmentation. arXiv preprint arXiv:2003.10304.

Gharaei, A., Hoseini Shekarabi, S. A., & Karimi, M. (2020). Modelling and optimal lot-sizing of the replenishments in constrained, multi-product and bi-objective EPQ models with defective products: Generalised cross decomposition. *International Journal of Systems Science: Operations & Logistics*, *7*(3), 262–274.

Gharaei, A., Hoseini Shekarabi, S. A., Karimi, M., Pourjavad, E., & Amjadian, A. (2019). An integrated stochastic EPQ model under quality and green policies: generalised cross decomposition under the separability approach. *International Journal of Systems Science: Operations & Logistics*, 1–13.

Gharaei, A., Karimi, M., & Hoseini Shekarabi, S. A. (2020). Joint economic lot-sizing in multi-product multi-level integrated supply chains: Generalized benders decomposition. *International Journal of Systems Science: Operations & Logistics*, *7*(4), 309–325.

Gharaei, A., Karimi, M., & Shekarabi, S. A. H. (2019). An integrated multi-product, multi-buyer supply chain under penalty, green, and quality control polices and a vendor managed inventory with consignment stock agreement: The outer approximation with equality relaxation and augmented penalty algorithm. *Applied Mathematical Modelling*, *69*, 223–254.

Giri, B., & Masanta, M. (2020). Developing a closed-loop supply chain model with price and quality dependent demand and learning in production in a stochastic environment. *International Journal of Systems Science: Operations & Logistics*, *7*(2), 147–163.

Gozes, O., Frid-Adar, M., Greenspan, H., Browning, P. D., Zhang, H., Ji, W., et al. (2020). Rapid ai development cycle for the coronavirus (covid-19) pandemic: Initial results for automated detection & patient monitoring using deep learning ct image analysis. arXiv preprint arXiv:2003.05037.

Greenspan, H., Estépar, R. S. J., Niessen, W. J., Siegel, E., & Nielsen, M. (2020). Position paper on COVID-19 imaging and AI: from the clinical needs and technological challenges to initial AI solutions at the lab and national level towards a new era for AI in healthcare. *Medical Image Analysis*, Article 101800.

Gungor, M. A. (2021). A comparative study on wavelet denoising for high noisy CT images of COVID-19 disease. *Optik*, *235*, Article 166652.

Hall, L. O., Paul, R., Goldgof, D. B., & Goldgof, G. M. (2020). Finding covid-19 from chest x-rays using deep learning on a small dataset. arXiv preprint arXiv:2004.02060.

Hannun, A. Y., Rajpurkar, P., Haghpanahi, M., Tison, G. H., Bourn, C., Turakhia, M. P., et al. (2019). Cardiologist-level arrhythmia detection and classification in ambulatory electrocardiograms using a deep neural network. *Nature Medicine*, *25*(1), 65.

Harmon, S. A., Sanford, T. H., Xu, S., Turkbey, E. B., Roth, H., Xu, Z., et al. (2020). Artificial intelligence for the detection of COVID-19 pneumonia on chest CT using multinational datasets. *Nature Communications*, *11*(1), 1–7.

Hasab, A. A. (2020). COVID-19 screening by RT-PCR: an epidemiological modelling.

Hassantabar, S., Ahmadi, M., & Sharifi, A. (2020). Diagnosis and detecton of infected tissue of COVID-19 patients based on lung X-Ray image using convolutional neural network approaches. *Chaos, Solitons & Fractals*, Article 110170.

Hemdan, E. E.-D., Shouman, M. A., & Karar, M. E. (2020). Covidx-net: A framework of deep learning classifiers to diagnose covid-19 in x-ray images. arXiv preprint arXiv:2003.11055.

Iandola, F. N., Han, S., Moskewicz, M. W., Ashraf, K., Dally, W. J., & Keutzer, K. (2016). Squeezenet: Alexnet-level accuracy with 50x fewer parameters and <0.5 MB model size. arXiv preprint arXiv:1602.07360.

Inturi, V., Sabareesh, G., & Penumakala, P. (2020). Bearing fault severity analysis on a multi-stage gearbox subjected to fluctuating speeds. *Experimental Techniques*.
Kanne, J. P. (2020). Chest CT findings in 2019 novel coronavirus (2019-nCoV) infections from Wuhan, China: key points for the radiologist.
Khan, A. I., Shah, J. L., & Bhat, M. M. (2020). Coronet: A deep neural network for detection and diagnosis of COVID-19 from chest x-ray images. *Computer Methods and Programs in Biomedicine*, Article 105581.
Kumar Singh, V., Abdel-Nasser, M., Pandey, N., & Puig, D. (2021). Lunginfseg: Segmenting covid-19 infected regions in lung ct images based on a receptive-field-aware deep learning framework. *Diagnostics*, *11*(2), 158.
Lee, E. Y., Ng, M.-Y., & Khong, P.-L. (2020). COVID-19 pneumonia: what has CT taught us? *The Lancet Infectious Diseases*, *20*(4), 384–385.
Li, L., Qin, L., Xu, Z., Yin, Y., Wang, X., Kong, B., et al. (2020). Artificial intelligence distinguishes COVID-19 from community acquired pneumonia on chest CT. *Radiology*.
Long, C., Xu, H., Shen, Q., Zhang, X., Fan, B., Wang, C., et al. (2020). Diagnosis of the coronavirus disease (COVID-19): rRT-PCR or CT? *European Journal of Radiology*, Article 108961.
Luengo-Oroz, M., Pham, K. H., Bullock, J., Kirkpatrick, R., Luccioni, A., Rubel, S., et al. (2020). Artificial intelligence cooperation to support the global response to COVID-19. *Nature Machine Intelligence*, 1–3.
Ma, J. (2020). Coronavirus: China's first confirmed Covid-19 case traced back to november 17. (13 March 2020) China / Society.
Ma, N., Zhang, X., Zheng, H.-T., & Sun, J. (2018). Shufflenet v2: Practical guidelines for efficient cnn architecture design. In *Proceedings of the European conference on computer vision* (pp. 116–131).
Mei, X., Lee, H.-C., Diao, K.-y., Huang, M., Lin, B., Liu, C., et al. (2020). Artificial intelligence–enabled rapid diagnosis of patients with COVID-19. *Nature Medicine*, 1–5.
Minaee, S., Kafieh, R., Sonka, M., Yazdani, S., & Soufi, G. J. (2020). Deep-covid: Predicting covid-19 from chest x-ray images using deep transfer learning. arXiv preprint arXiv:2004.09363.
Mitsuhashi, H., & Greve, H. R. (2009). A matching theory of alliance formation and organizational success: Complementarity and compatibility. *Academy of Management Journal*, *52*(5), 975–995.
Narin, A., Kaya, C., & Pamuk, Z. (2020). Automatic detection of coronavirus disease (covid-19) using x-ray images and deep convolutional neural networks. arXiv preprint arXiv:2003.10849.
Nazarahari, M., Namin, S. G., Markazi, A. H. D., & Anaraki, A. K. (2015). A multi-wavelet optimization approach using similarity measures for electrocardiogram signal classification. *Biomedical Signal Processing and Control*, *20*, 142–151.
Organization, W. H. (2020). *Novel Coronavirus(2019-nCoV) situation report-166*: *Tech. rep.*, World Health Organization.
Ozturk, T., Talo, M., Yildirim, E. A., Baloglu, U. B., Yildirim, O., & Acharya, U. R. (2020). Automated detection of COVID-19 cases using deep neural networks with X-ray images. *Computers in Biology and Medicine*, Article 103792.
Patchsung, M., Jantarug, K., Pattama, A., Aphicho, K., Suraritdechachai, S., Meesawat, P., et al. (2020). Clinical validation of a Cas13-based assay for the detection of SARS-CoV-2 RNA. *Nature Biomedical Engineering*, 1–10.
Praveen, G., Vamsi, I., Suresh, K., & Radhika, S. (2020). Evaluation of surface roughness in incremental forming using image processing based methods. *Measurement*, Article 108055.
Rabbani, M., Hosseini-Mokhallesun, S. A. A., Ordibazar, A. H., & Farrokhi-Asl, H. (2020). A hybrid robust possibilistic approach for a sustainable supply chain location-allocation network design. *International Journal of Systems Science: Operations & Logistics*, *7*(1), 60–75.
Radhika, S., Sabareesh, G., Jagadanand, G., & Sugumaran, V. (2010). Precise wavelet for current signature in 3ϕ IM. *Expert Systems with Applications*, *37*(1), 450–455.
Radhika, S., Tamura, Y., & Matsui, M. (2012). Use of post-storm images for automated tornado-borne debris path identification using texture-wavelet analysis. *Journal of Wind Engineering and Industrial Aerodynamics*, *107*, 202–213.
Radhika, S., Tamura, Y., & Matsui, M. (2015). Cyclone damage detection on building structures from pre-and post-satellite images using wavelet based pattern recognition. *Journal of Wind Engineering and Industrial Aerodynamics*, *136*, 23–33.
Rajpal, S., Lakhyani, N., Singh, A. K., Kohli, R., & Kumar, N. (2021). Using handpicked features in conjunction with ResNet-50 for improved detection of COVID-19 from chest X-ray images. *Chaos, Solitons & Fractals*, *145*, Article 110749.
Rajpurkar, P., Irvin, J., Zhu, K., Yang, B., Mehta, H., Duan, T., et al. (2017). Chexnet: Radiologist-level pneumonia detection on chest x-rays with deep learning. arXiv preprint arXiv:1711.05225.
Rodriguez, J. D., Perez, A., & Lozano, J. A. (2009). Sensitivity analysis of k-fold cross validation in prediction error estimation. *IEEE Transactions on Pattern Analysis and Machine Intelligence*, *32*(3), 569–575.
Salman, F. M., Abu-Naser, S. S., Alajrami, E., Abu-Nasser, B. S., & Alashqar, B. A. (2020). Covid-19 detection using artificial intelligence. *International Journal of Academic Engineering Research*, *4*(3), 18–25.
Sengupta, A., Ye, Y., Wang, R., Liu, C., & Roy, K. (2019). Going deeper in spiking neural networks: Vgg and residual architectures. *Frontiers in Neuroscience*, *13*, 95.
Sethy, P. K., & Behera, S. K. (2020). Detection of coronavirus disease (covid-19) based on deep features. (p. 2020). Preprints 2020030300.
Shi, H., Han, X., Jiang, N., Cao, Y., Alwalid, O., Gu, J., et al. (2020). Radiological findings from 81 patients with COVID-19 pneumonia in Wuhan, China: a descriptive study. *The Lancet Infectious Diseases*.
Shibly, K. H., Dey, S. K., Islam, M. T. U., & Rahman, M. M. (2020). COVID Faster R-CNN: A novel framework to diagnose novel coronavirus disease (COVID-19) in X-Ray images. MedRxiv.
Sohrabi, C., Alsafi, Z., O'Neill, N., Khan, M., Kerwan, A., Al-Jabir, A., et al. (2020). World health organization declares global emergency: A review of the 2019 novel coronavirus (COVID-19). *International Journal of Surgery*.
Song, F., Shi, N., Shan, F., Zhang, Z., Shen, J., Lu, H., et al. (2020). Emerging coronavirus 2019-nCoV pneumonia. *Radiology*.
Song, Y., Zheng, S., Li, L., Zhang, X., Zhang, X., Huang, Z., et al. (2020). Deep learning enables accurate diagnosis of novel coronavirus (COVID-19) with CT images. MedRxiv.
Souza, J. C., Diniz, J. O. B., Ferreira, J. L., da Silva, G. L. F., Silva, A. C., & de Paiva, A. C. (2019). An automatic method for lung segmentation and reconstruction in chest X-ray using deep neural networks. *Computer Methods and Programs in Biomedicine*, *177*, 285–296.
Szegedy, C., Ioffe, S., Vanhoucke, V., & Alemi, A. (2016). Inception-v4, inception-resnet and the impact of residual connections on learning. arXiv preprint arXiv:1602.07261.
Tabik, S., Gómez-Ríos, A., Martín-Rodríguez, J. L., Sevillano-García, I., Rey-Area, M., Charte, D., et al. (2020). COVIDGR dataset and COVID-SDNet methodology for predicting COVID-19 based on Chest X-Ray images. *IEEE Journal of Biomedical and Health Informatics*, *24*(12), 3595–3605.
Talo, M., Yildirim, O., Baloglu, U. B., Aydin, G., & Acharya, U. R. (2019). Convolutional neural networks for multi-class brain disease detection using MRI images. *Computerized Medical Imaging and Graphics*, *78*, Article 101673.
Ting, D. S. W., Carin, L., Dzau, V., & Wong, T. Y. (2020). Digital technology and COVID-19. *Nature Medicine*, *26*(4), 459–461.
Tsao, Y.-C. (2015). Design of a carbon-efficient supply-chain network under trade credits. *International Journal of Systems Science: Operations & Logistics*, *2*(3), 177–186.
Vamsi, I., Sabareesh, G., & Penumakala, P. (2019). Comparison of condition monitoring techniques in assessing fault severity for a wind turbine gearbox under non-stationary loading. *Mechanical Systems and Signal Processing*, *124*, 1–20.
Verma, A. K., Nagpal, S., Desai, A., & Sudha, R. (2020). An efficient neural-network model for real-time fault detection in industrial machine. *Neural Computing and Applications*, 1–14.
Wang, J., & Du, Z. (2019). A method of processing color image watermarking based on the haar wavelet. *Journal of Visual Communication and Image Representation*, *64*, Article 102627.
Wang, S., Kang, B., Ma, J., Zeng, X., Xiao, M., Guo, J., et al. (2020). A deep learning algorithm using CT images to screen for Corona Virus Disease (COVID-19). MedRxiv.
Wang, S.-H., Nayak, D. R., Guttery, D. S., Zhang, X., & Zhang, Y.-D. (2020). COVID-19 classification by CCSHNet with deep fusion using transfer learning and discriminant correlation analysis. *Information Fusion*, *68*, 131–148.
Wang, L., & Wong, A. (2020). COVID-Net: A tailored deep convolutional neural network design for detection of COVID-19 cases from chest X-Ray images. arXiv preprint arXiv:2003.09871.
Wang, W., Xu, Y., Gao, R., Lu, R., Han, K., Wu, G., et al. (2020). Detection of SARS-CoV-2 in different types of clinical specimens. *Jama*, *323*(18), 1843–1844.
Wang, S., Zha, Y., Li, W., Wu, Q., Li, X., Niu, M., et al. (2020). A fully automatic deep learning system for COVID-19 diagnostic and prognostic analysis. *European Respiratory Journal*.
W. H. O. (2020). COVID-19 symptoms. https://www.who.int/health-topics/coronavirus.
Worldometer (2020). Worldometer coronavirus. https://www.worldmeters.info/coronavirus/countries-where-coronavirushas-spread/.
Xie, S., Zheng, X., Chen, Y., Xie, L., Liu, J., Zhang, Y., et al. (2018). Artifact removal using improved GoogLeNet for sparse-view CT reconstruction. *Scientific Reports*, *8*(1), 1–9.
Xu, X., Jiang, X., Ma, C., Du, P., Li, X., Lv, S., et al. (2020). A deep learning system to screen novel coronavirus disease 2019 pneumonia. *Engineering*.
Zhang, Y.-D., Satapathy, S. C., Zhu, L.-Y., Górriz, J. M., & Wang, S.-H. (2020). A seven-layer convolutional neural network for chest CT based COVID-19 diagnosis using stochastic pooling. *IEEE Sensors Journal*.
Zhang, J., Xie, Y., Li, Y., Shen, C., & Xia, Y. (2020). Covid-19 Screening on chest x-ray images using deep learning based anomaly detection. arXiv preprint arXiv:2003.12338.
Zheng, C., Deng, X., Fu, Q., Zhou, Q., Feng, J., Ma, H., et al. (2020). Deep learning-based detection for COVID-19 from chest CT using weak label. MedRxiv.